

How does Radiation Reaction Affect Relativistic Magnetized Shocks Emission

Yu Zhang¹, Yuanpei Yang², Liangliang Ji^{1*}

¹ State Key Laboratory of High Field Laser Physics and CAS Center for Excellence in Ultra-intense Laser Science, Shanghai Institute of Optics and Fine Mechanics (SIOM), Chinese Academy of Sciences (CAS), Shanghai, China

²South-Western Institute for Astronomy Research, Yunnan University, Kunming, China

*Contact Author: jill@siom.ac.cn

Abstract

Relativistic magnetized shocks, through the Synchrotron Maser Instability (SMI) mechanism, represent a promising framework for generating coherent radiations, potentially accounting for the enigmatic Fast Radio Bursts (FRBs)—cosmic radio transients with extreme luminosity. This study investigates how the radiation reaction (RR) effect, induced by high-energy photon emissions during SMI, significantly modifies particle dynamics and emission properties in magnetized shocks. Through comprehensive Particle-In-Cell (PIC) simulations, we demonstrate that RR effects fundamentally alter coherent cyclotron motion at shock fronts, producing distinct observational signatures: spectral broadening, peak frequency upshift, and enhanced radiation intensity. Our findings suggest that RR-mediated magnetized shocks could provide a natural explanation for the bimodal energy distribution observed in repeating FRB 121102 and the positive correlation of luminosity-bandwidth between repeating and one-off FRBs in CHIME/FRB catalog. These results support the magnetized shock as a viable source of FRBs.

Introduction

Fast radio bursts (FRBs) are luminous, millisecond-duration astrophysical transients with GHz frequencies, typically of extragalactic origin[1-7]. Their extreme brightness temperatures suggest a coherent emission mechanism, but the precise generation process of FRBs remains unresolved yet. Current theories predominantly favor magnetars as the central engines powering FRBs, a view bolstered by the observation of the Galactic FRB 200428 linked to a magnetar[8,9].

In magnetar environments, FRBs may originate from relativistic plasma instabilities[10] or coherent electron beam curvature radiation[11-15] within the magnetosphere, or from relativistic magnetized shocks[16-23] externally. The latter, often driven by magnetar flare ejecta colliding with magnetized winds, can produce coherent electromagnetic radiation through "synchrotron maser instability (SMI)"[20,24,25] -- Cold, magnetized particles entering the shock collectively accelerate and undergo synchrotron-like motion at the shock front, emitting coherent electromagnetic pulses, known as "precursor waves" that propagate upstream. The emission process of magnetized shocks can be quantitatively studied using kinetic particle-in-cell (PIC)

simulation programs[20-22]. Studies on electron-positron shock radiation[19-21] show that magnetized shock models can explain the features of FRBs like coherence, duration, polarization and spectrum under external magnetospheric parameters, but the radiation efficiency $\sim 7 \times 10^{-4}/\sigma^2$ struggles to account for FRB's extreme luminosity in the context of magnetar winds with $\sigma \sim (10 - 100)$ [23], here σ is the magnetization, defines as the ratio of Poynting flux to particle energy flux of the pre-shock flow. Recent studies on electron-ion shocks[22], with $m_{ion}/m_e = 1/200$, reveal that ion involvement allows precursor waves to generate wake-fields upstream, accelerating electrons and boosting energy conversion efficiency to $\sim 10^{-3}$ even at $\sigma = 100$, thereby adequately accounting for FRB luminosity.

Given FRBs' enormous isotropic luminosity $L \sim (10^{38} - 10^{46})$ erg/s [7,8,26,27], the normalized field near source can be estimated as¹ $a_0 \sim 10^4 L_{44}^{1/2} R_{10}^{-1} \omega_{10}^{-1}$, where R is FRBs' transport distance from the source, ω is the angular frequency. During radiation or initial propagation near the source, electrons/positrons in such a strong field are expected

¹ the convention $Q_x = Q/10^x$ is adopted in cgs units unless otherwise specified.

to undergo significant acceleration, reaching Lorentz factors $\gamma \sim a_0^2$, and emit considerable amounts of photons. The latter is supported by the hard X/soft γ bursts observation associated with the galactic FRB200428[28-31]. The radiation damping could induce non-negligible recoiling on electrons, known as the Radiation Reaction (RR) effect[32]. For GHz wave, the threshold field for RR dominance can be estimated as $a_{\text{thr}} \sim (3\lambda_{\text{GHz}}/4\pi r_e)^{1/3} \sim 2.94 \times 10^4$, where $\lambda_{\text{GHz}} \sim 30$ cm is the wavelength of 1GHz radio wave, $r_e \sim 2.82 \times 10^{-13}$ cm is the classical electron radius. Thus, it is highly probable that the most powerful FRBs or those closest to the magnetosphere could trigger the RR effect during radiation.

Previous studies established that magnetized shocks producing FRBs must lie beyond $\sim 10^{13}$ cm from the magnetar core to avoid radiation disruption by RR effects from strong precursor waves and upstream particles[33]. This work systematically investigates RR's direct influence on shock-mediated radiation mechanisms. The shock structure, radiation intensity, and spectral properties in SMI fundamentally depend on coherent electron-positron gyration at shock fronts. Given a 1D-PIC simulation², we demonstrate that RR-induced modifications to particle motion can substantially alter SMI characteristics, leading to higher peak frequency, wider bandwidth, stronger intensity and enhanced energy efficiency. Incorporating the RR effect, the magnetized shock model can naturally generate electromagnetic radiation with distinct energy distribution modes, which allows it to account for the bimodal energy distribution identified in repeating FRB 20121102A[34], with its bandwidth differences between high/low energy modes supporting our conclusions [35]. Notably, similar bimodal energy spectra have been indicated in repeating FRB 20200120E[36] and FRB 20201124A[37], suggesting the potential universality of the two-component energy function in repeating FRBs. The energy-bandwidth statistical positive correlation observed in repeating and one-off FRBs of CHIME/FRB also aligns with our conclusion[38,39].

Methods

We employed an open-source PIC code SMILEI-1D[40] to simulate the magnetized shock's generation and evolution induced by an ultra-relativistic e^-/e^+ jet with magnetization σ , e^-/e^+ number density n_e , and a bulk Lorentz factor γ_0 . The simulation was accomplished in the

² As a quasi-one-dimensional process, SMI's spectral characteristics and energy conversion efficiency can be examined through 1D PIC simulations. The 1D-PIC calculations are consistent with 3D-PIC results, the latter additionally reveal the evolution of radiation polarization.

downstream frame. The jet enters from the right side of the simulation box along the $-\hat{x}$ direction and, after being reflected at the wall located at $x = 0$, collides with the incident flow, launching a magnetized shock propagates along $+\hat{x}$. The pre-shock jet carries a frozen magnetic field $\mathbf{B}_0 \sim B_0 \hat{z}$ and a motional electric field $\mathbf{E}_0 \sim -\beta_0 B_0 \hat{y}$, where $\beta_0 = \sqrt{1 - 1/\gamma_0^2}$. Our simulation employed 100 particles per species per cell, spatial resolution $\Delta x = \frac{1}{128} c/\omega_p$, and time step $\Delta t = 0.99 \Delta x$. The spatial domain ranges $0 < x < 2000 c/\omega_p$, and the total time after the shock forming is $2000 \omega_p^{-1}$.

For the calculation of the RR effect, we adopted Landau-Lifshitz (LL) method provided by SMILEI code, which incorporated the RR force \mathbf{F}_{rr} in LL form[41] into the particle motion equation. For free electron in electromagnetic wave field,

$$\mathbf{F}_{rr} \approx -(2e^4/3m_e^2 c^5) \gamma^2 \mathbf{v} [(\mathbf{E} + \mathbf{v} \times \mathbf{B}/c)^2 - (\mathbf{E} \cdot \mathbf{v})^2/c^2]$$
Here \mathbf{E} and \mathbf{B} are electric and magnetic field, respectively. γ and \mathbf{v} are e^-/e^+ 's Lorentz factor and velocity, c is the light speed. As a quantum electrodynamics (QED) effect, the intensity of the RR effect on shock front can be measured by the QED factor χ

$$\chi \approx (\gamma_0/E_s) \sqrt{(\mathbf{E} + \boldsymbol{\beta}_0 \times \mathbf{B})^2 - (\boldsymbol{\beta}_0 \cdot \mathbf{E})^2} \sim 2\gamma_0 B_0/E_s$$
where $E_s = 1.32 \times 10^{16}$ V/cm is the Schwinger field, $\mathbf{E} \sim \beta_0 B_0 \hat{y}$ and $\mathbf{B} \sim 3B_0 \hat{z}$ are typical electric and magnetic field at shock front in high magnetization ($\sigma > 1$). Combining the definition of $\sigma = B_0^2/(8\pi\gamma_0 N_0 m_e c^2) = \omega_c^2/\omega_p^2$, one can get $\chi = 2 \times 10^{-16} (\sigma \gamma_0^3 n_e/\text{cm}^{-3})^{1/2}$, here e is the electron charge, m_e is the electron mass, $\omega_c = eB_0/\gamma_0 m_e c$ is electron's cyclotron frequency, $\omega_p = (8\pi n_e e^2/\gamma_0 m_e)^{1/2}$ is the upstream plasma frequency. When χ approaches 1, intense gamma ray e^-/e^+ pair cascades would be produced, our calculations show radiation damping causes substantial energy loss for e^-/e^+ even at $\chi \sim 10^{-3}$. The computations in this paper initially selected (γ_0, σ, n_e) as $(2 \times 10^4, 10, 1.38 \times 10^{12} \text{cm}^{-3})$, which correspond to $\chi = 2.2 \times 10^{-3}$. By the way, we compared the LL and Monte Carlo (MC) methods in SMILEI for radiation damping calculations. The LL method overestimates radiative damping compared to MC when $\chi \gtrsim 0.01$, amplifying radiation reaction effects. However, for $\chi \sim 10^{-3}$ as in this study, both methods yield similar results. All subsequent simulations are based on the LL method.

Results

The simulation reveals that the RR effect mainly acts in two stages: the counter-propagation between the upstream particle flow and the precursor wave, and the shock front area.

For the former stage, under the precursor wave field, the upstream particles oscillate transversely to generate high-energy radiation. The radiation damping continues until the RR effect cannot be triggered anymore and then the particles' energy reaches saturation, as shown in Fig. 1. The simulation is conducted in the downstream reference frame. In the upstream frame, initially stationary or non-relativistic particles are accelerated by the γ_0 -boosted precursor wave fields, then emit high-energy photons via transverse oscillations until reaching a critical saturation energy where RR ceases. As the QED factor χ is Lorentz invariant, the radiation reaction intensity remains consistent across both reference frames.

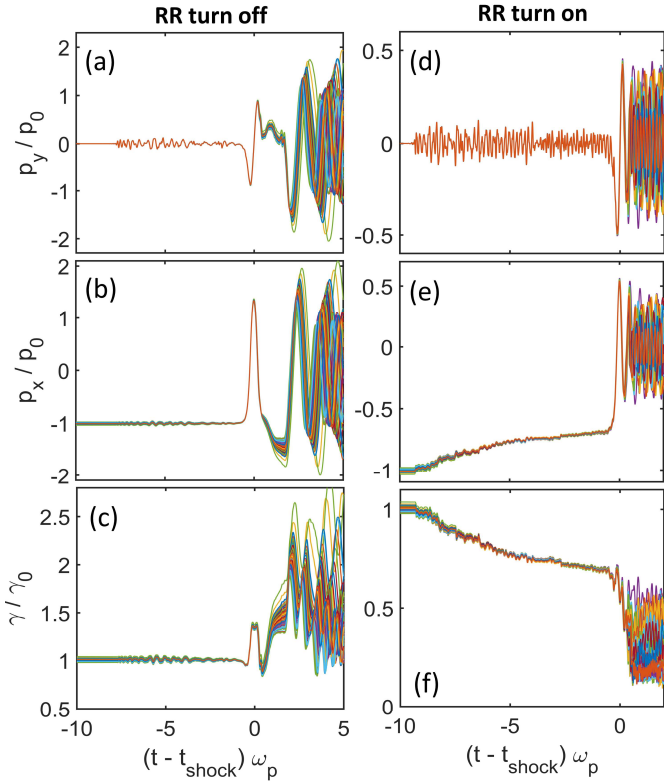


FIG.1 the temporal evolution of electron flow's momentum components and Lorentz factor. Panels (a)-(c) display the trajectories of 100 adjacent electrons in terms of the transverse momentum p_x , longitudinal momentum p_y , and Lorentz factor γ with the RR module disabled. Here $p_0 = (\gamma_0^2 - 1)^{1/2}$, t_{shock} is the time moment marking upstream particles' entry into the shock. The corresponding distributions with the RR module enabled under identical parameters are presented in panels (d)-(f), respectively.

In the later stage, as the particle flow encounters the shock, the RR effect is reinitiated by the solitary electromagnetic peak at the shock front. This leads to three distinct effects on the electron flow's coherent cyclotron motion, illustrated in Fig. 2(d): (1) The particle flow's energy progressively diminishes, causing the cyclotron radius in momentum space

to shrink continuously. (2) The cyclotron period $T \sim 2\pi\gamma m_e/eB_0$ shortens, increasing the number of coherent cyclotron turns before thermalization, with the trajectory adopting a spiral pattern. Here γ denotes the bulk Lorentz factor of the electron/positron flow upon shock entry. (3) Shock acceleration's energy gain is balanced by radiation damping, leading to a more gradual energy change in the particle flow.

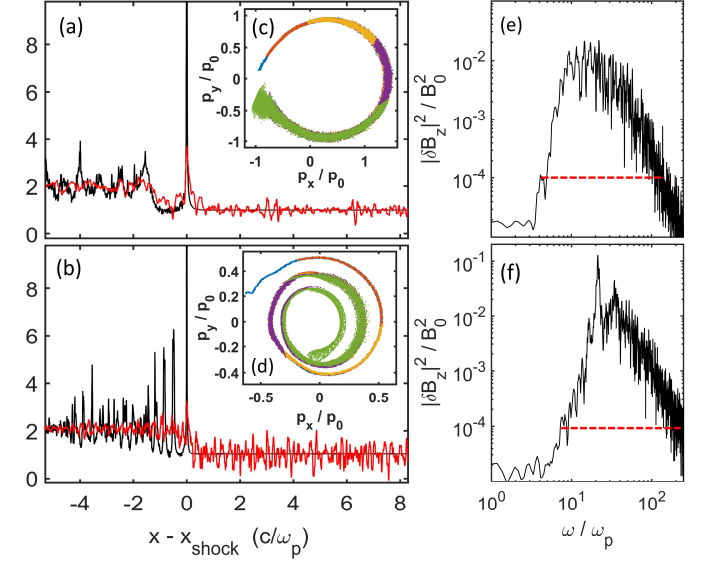


FIG.2 (a) and (b) show the spatial distribution of density and magnetic field around the shock front with RR disabled and enabled, respectively. Black lines represent the normalized electron density n_e/n_{e0} , and red lines represent the magnetic field B_z/B_0 . (c) and (d) display sequential temporal snapshots of positron flow dynamics in momentum space during shock entry prior to thermalization. The temporal evolution is color-coded, with blue, red, yellow, purple, and green markers representing progressively later time points at $20 \Delta t$ intervals. (e) and (f) are spectrum of $|\delta B_z|^2/B_0^2$ ahead of the shock front with RR module turned off and on. The spectra are normalized as $\int |\delta B_z(\omega)|^2/B_0^2 d\omega = \langle \delta B_z^2 \rangle/B_0^2$, $\delta B_z = B_z - B_0$.

The RR effect-induced modifications in particle motion have substantially reshaped the shock structure. The particle flow's multiple coherent cyclotron motions result in the emergence of several density peaks at the shock front, as depicted in Fig. 2(b), and significantly influence the maser radiation spectrum. When the RR effect is neglected, the spectral distribution ahead of the shock aligns with Plotnikov & Sironi (2019)'s simulation results[21], as illustrated in Fig. 2(c). For $\sigma = 10$, the cutoff frequency $\omega_{\text{cutoff}} \sim 3.3\omega_p$ and the peak frequency $\omega_{\text{peak}} \sim 12\omega_p$ closely correspond to the theoretical predictions for $\omega_{\text{cutoff}} \sim \omega_c = \sqrt{\sigma}\omega_p$ and $\omega_{\text{peak}} \sim (3-4)\omega_c$ [20,21].

When the RR effect is included, the spectral distribution of the maser radiation is depicted in Fig. 2(f). Correlating the

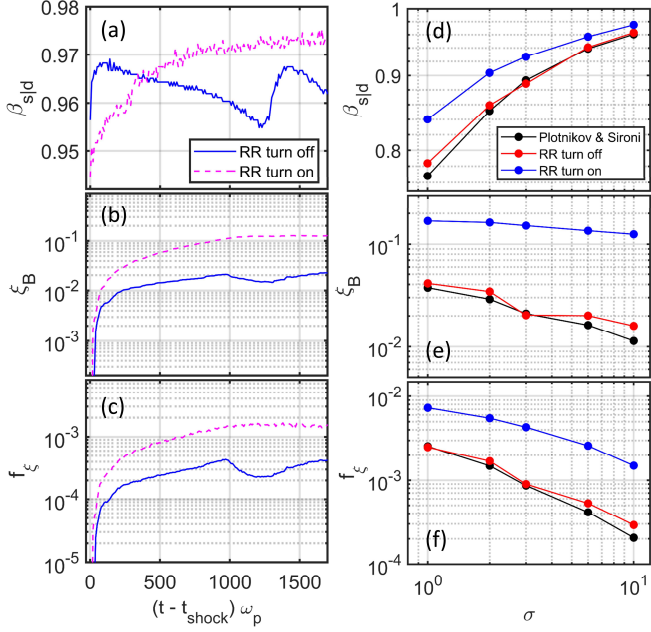


FIG.3 (a), (b) and (c) represents the temporal evolution of shock velocity $\beta_{s|d}$, precursor wave intensity ξ_B and the energy radio efficiency f_ξ measured in downstream rest frame, respectively. The blue solid line and magenta dashed line represent the RR module-off and RR module-on cases, respectively. (d), (e) and (f) shows the $\beta_{s|d}$, ξ_B and f_ξ 's evolution over σ measured in downstream frame with fixed QED factor $\chi = 2.2 \times 10^{-3}$ (precisely, fixed $\gamma_0 = 2 \times 10^4$ and $\sigma n_e = 1.38 \times 10^{13}$). The black, red, and blue dots denote the results from Plotnikov & Sironi (2019) [21], RR module-off, and RR module-on conditions, respectively.

alterations with the particle cyclotron's momentum trajectory in Fig. 2(d), the primary modifications are as follows:

(1) Higher ω_{cutoff} and ω_{peak} . As shown in Fig. 1(f), upstream energy depletion decreases the particle stream's Lorentz factor at shock entry, consequently elevating both ω_{cutoff} and ω_{peak} , which are proportional to $\omega_c = eB_0/\gamma m_e$. In this case, $\gamma \sim 0.6 \gamma_0$ upon shock entry, resulting in $\omega_{\text{cutoff}} \sim 5.8\omega_p$ and $\omega_{\text{peak}} \sim 21\omega_p$, approximately doubling the values observed without RR effects.

(2) Broader frequency bandwidth. During the coherent cyclotron process, the radiation frequency increases as the particle flow's energy continuously decreases, leading to broader frequency bandwidth. The red dashed lines in Fig. 2(e) and (f) mark the frequency range Δf_{1e-4} where the radiation intensity $|\delta B_z|^2/B_0^2 > 10^{-4}$. Here without considering RR, $\Delta f_{1e-4} \sim 130 \omega_p$, and with RR considered, $\Delta f_{1e-4} \sim 210 \omega_p$.

(3) The radiation intensity at peak frequency significantly increases, forming a distinct spectral peak. Without RR effects,

particles undergo acceleration followed by deceleration in the shock front's electrostatic field, as shown in Fig. 2(c). With RR effects, radiation damping counterbalances shock

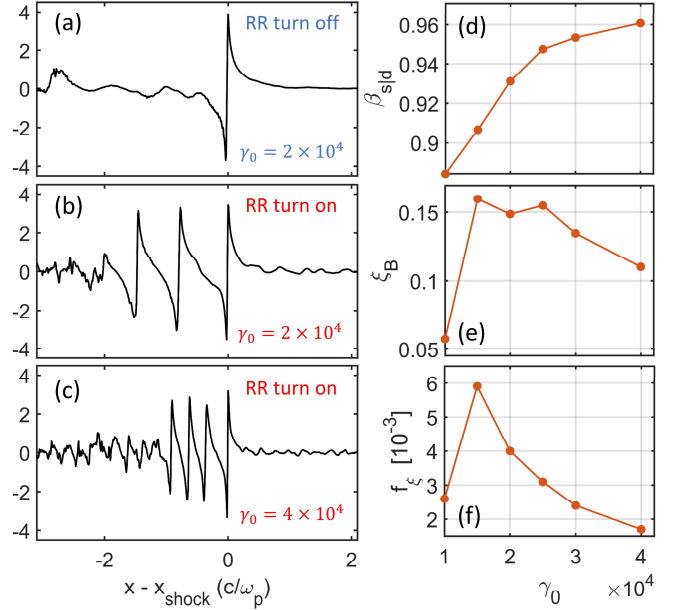


FIG.4 Fixing $\sigma = 3$ and $n_e = 4.6 \times 10^{13} \text{ cm}^{-3}$, the evolution of SMI with γ_0 (i.e. the evolution with χ). (a), (b) and (c) represents the transversal current density $J_y/en_e c$ around the shock front. Here in (a) $\gamma_0 = 2 \times 10^4$, without the RR module turned off. (b) $\gamma_0 = 2 \times 10^4$, without the RR module turned on. (c) $\gamma_0 = 4 \times 10^4$, without the RR module turned on. (d), (e) and (f) shows the evolution of $\beta_{s|d}$, ξ_B and f_ξ with γ_0 when the RR module turned on, respectively.

acceleration, resulting in smoother energy modulation during coherent cyclotron motion, particularly in the first orbit where particle coherence is strongest, leading to more concentrated frequency emission.

Interestingly, despite the RR effect reducing the particle flow energy at shock entry, it significantly enhances both the shock radiation intensity and energy conversion efficiency, as demonstrated in Fig. 3. Without the RR effect, our results for radiation intensity $\xi_B = \langle \delta B_z^2 \rangle / B_0^2$ and energy conversion efficiency $f_\xi = \xi_B \sigma (1 + \beta_{s|d}) / [(1 + \sigma)(\beta_0 + \beta_{s|d})]$ versus σ agree well with Plotnikov & Sironi (2019) [21]. However, when including RR effects, our simulations show 2 ~ 5 times enhancement in both ξ_B and f_ξ across $\sigma \sim (1 - 10)$, as shown in Figs. 3(e) and 3(f).

This phenomenon arises because particles retain highly relativistic energies upon shock entry despite upstream radiation damping (in this case, $\gamma \sim 0.6 \gamma_0 \gtrsim 10^4$). As shown in Figs. 4(a) and 4(c), the RR effect hardly affects the peak intensity of individual current pulses $J_{y,\text{peak}} \propto e(n_e - +$

$n_{e+})\beta c$ from coherent cyclotron motion, here $\beta = (1 - 1/\gamma^2)^{-1/2} \sim 1$. However, RR-induced shortening of the cyclotron period generates multiple coherent motions, producing superimposed current pulses whose upstream radiation constructively interferes, thereby enhancing total ξ_B .

At fixed σ and n_e , increasing γ_0 initially enhances the RR effect, extending the particle flow's coherent cyclotron turns and increasing ξ_B . However, when $\beta \sim 1$ is no longer maintained, the cyclotron-induced current pulses weaken, causing both ξ_B and f_ξ to decrease, as demonstrated in Figs. 4(e) and (f). While within our simulations, RR activation yields consistently higher values than RR-off cases: $\xi_B \sim 0.021$ and $f_\xi \sim 8.64 \times 10^{-4}$, both showing γ_0 -independence, as observed in former magnetized shock simulation[20,21].

Based on the above discussions, the RR effect changes the observable characteristic of SMI in both the spectrum and energy aspects. In spectrum, it raises the peak frequency, broadens the bandwidth, and forms a peak spectral structure. In energy, it significantly boosts the radiation intensity.

Our analysis of observational characteristics suggests that for FRBs generated through the SMI mechanism, a positive correlation exists between luminosity and both bandwidth and peak frequency, particularly evident in large-scale statistical analyses. This correlation is substantiated by distinct statistical patterns observed in the CHIME/FRB catalog, where one-off FRBs consistently demonstrate higher luminosity and broader frequency bandwidths compared to their repeating counterparts[38,39].

Furthermore, the RR effect's enhancement of SMI radiation intensity provides a natural mechanism for generating electromagnetic emissions with distinct energy patterns, accounting for the observed bimodal energy spectrum in repeating FRB 20121102A[34]. This phenomenon appears to extend to other repeating FRBs, including 20200120E[36] and 20201124A[37], suggesting a potential universality of bimodal spectral distributions among repeating FRBs. Statistical analysis of FRB 20121102A's spectral characteristics reveals that high-energy mode bursts consistently exhibit broader bandwidths than their low-energy counterparts[35]. a finding that aligns precisely with our theoretical predictions.

Conclusion

This study employs 1D-PIC simulations to investigate the RR effect on magnetized shock radiation, revealing its significant impact on particle dynamics and emission characteristics. Our findings demonstrate that the RR effect

fundamentally alters coherent cyclotron motion at shock fronts, resulting in distinct modifications: peak frequency upshift, bandwidth broadening, characteristic peak spectral morphology, and enhanced radiation intensity. These results provide the first comprehensive simulation-based physical description of RR-mediated magnetized shock radiation, establishing clear observational signatures of RR-affected shock processes.

Importantly, RR-incorporated shock radiation model could provide natural explanation of the two key observational phenomena: (1) the bimodal energy distribution in repeating FRB 20121102A. (2) the systematic luminosity-bandwidth correlation distinguishing repeating and one-off FRBs in the CHIME/FRB catalog.

Reference

- [1] J. M. Cordes and S. Chatterjee, *Annu Rev Astron Astr* **57**, 417 (2019).
- [2] D. R. Lorimer, *Nat Astron* **2**, 860 (2018).
- [3] E. Petroff, J. W. T. Hessels, and D. R. Lorimer, *Astron Astrophys Rev* **27** (2019).
- [4] E. Platts, A. Weltman, A. Walters, S. P. Tendulkar, J. E. B. Gordin, and S. Kandhai, *Phys. Rep.* **821**, 1 (2019).
- [5] J. I. Katz, *Prog. Part. Nucl. Phys* **103**, 1 (2018).
- [6] S. B. Popov, K. A. Postnov, and M. S. Pshirkov, *Phys-Usp+* **61**, 965 (2018).
- [7] B. Zhang, *Nature* **587**, 45 (2020).
- [8] C. D. Bochenek, V. Ravi, K. V. Belov, G. Hallinan, J. Kocz, S. R. Kulkarni, and D. L. McKenna, *Nature* **587**, 59 (2020).
- [9] B. C. Andersen *et al.*, *Nature* **587**, 54 (2020).
- [10] Y. Lyubarsky, *Astrophys J* **897** (2020).
- [11] P. Kumar and Z. Bosnjak, *Mon. Not. R. Astron. Soc.* **494**, 2385 (2020).
- [12] W. B. Lu, P. Kumar, and B. Zhang, *Mon. Not. R. Astron. Soc.* **498**, 1397 (2020).
- [13] Y. P. Yang and B. Zhang, *Astrophys J* **868** (2018).
- [14] W. Lu and P. Kumar, *Mon. Not. R. Astron. Soc.* **477**, 2470 (2018).
- [15] Y. P. Yang, J. P. Zhu, B. Zhang, and X. F. Wu, *Astrophys J Lett* **901** (2020).
- [16] Y. Lyubarsky, *Mon. Not. R. Astron. Soc.* **442**, L9 (2014).
- [17] A. M. Beloborodov, *Astrophys J Lett* **843** (2017).
- [18] E. Waxman, *Astrophys J* **842** (2017).
- [19] L. Sironi, B. Margalit, and B. D. Metzger, *Mon. Not. R. Astron. Soc.* **485**, 4091 (2019).
- [20] L. Sironi, I. Plotnikov, J. Nättilä, and A. M. Beloborodov, *Phys. Rev. Lett.* **127** (2021).
- [21] I. Plotnikov and L. Sironi, *Mon. Not. R. Astron. Soc.*

485, 3816 (2019).

[22] M. Iwamoto, Y. Matsumoto, T. Amano, S. Matsukiyo, and M. Hoshino, *Phys. Rev. Lett.* **132** (2024).

[23] A. M. Beloborodov, *Astrophys J* **896** (2020).

[24] D. Alsop and J. Arons, *Phys. Fluids* **31**, 839 (1988).

[25] M. Hoshino and J. Arons, *Phys Fluids B-Plasma* **3**, 818 (1991).

[26] V. Ravi *et al.*, *Nature* **572**, 352 (2019).

[27] B. Zhang, *Astrophys J Lett* **867** (2018).

[28] A. Ridnaia *et al.*, *Nat Astron* **5**, 372 (2021).

[29] C. K. Li *et al.*, *Nat Astron* **5**, 378 (2021).

[30] M. Tavani *et al.*, *Nat Astron* **5**, 401 (2021).

[31] S. Mereghetti *et al.*, *Astrophys J Lett* **898** (2020).

[32] Y. B. Zeldovich, *Sov. Phys. Usp.* **115**, 161 (1975).

[33] W. Lu and P. Kumar, *Mon. Not. R. Astron. Soc.* **494**, 1217 (2020).

[34] D. Li *et al.*, *Nature* **598**, 267 (2021).

[35] S.-Q. Zhong, W.-J. Xie, C.-M. Deng, L. Li, Z.-G. Dai, and H.-M. Zhang, *Astrophys J* **926** (2022).

[36] S. B. Zhang *et al.*, *Nat. Commun.* **15** (2024).

[37] F. Kirsten *et al.*, *Nat Astron* **8**, 337 (2024).

[38] H.-Y. Chen, W.-M. Gu, M. Sun, and T. Yi, *Astrophys J* **939** (2022).

[39] Z. Pleunis *et al.*, *Astrophys J* **923** (2021).

[40] J. Derouillat *et al.*, *Comput. Phys. Commun.* **222**, 351 (2018).

[41] L. D. Landau and E. M. Lifshitz, *The Classical Theory of Fields* (Pergamon Press, Oxford, 1971).